

A unified Green's function approach for spectral and thermodynamic properties from algorithmic inversion of dynamical potentials

Tommaso Chiarotti,^{1,*} Nicola Marzari,¹ and Andrea Ferretti²

¹*Theory and Simulations of Materials (THEOS) and National Centre for Computational Design and Discovery of Novel Materials (MARVEL), École Polytechnique Fédérale de Lausanne, 1015 Lausanne, Switzerland*

²*Centro S3, CNR-Istituto Nanoscienze, 41125 Modena, Italy*

(Dated: September 17, 2021)

Dynamical potentials appear in many advanced electronic-structure methods, including self-energies from many-body perturbation theory, dynamical mean-field theory, electronic-transport formulations, and many embedding approaches. Here, we propose a novel treatment for the frequency dependence, introducing an algorithmic inversion method that can be applied to dynamical potentials expanded as sum over poles. This approach allows for an exact solution of Dyson-like equations at all frequencies via a mapping to a matrix diagonalization, and provides simultaneously frequency-dependent (spectral) and frequency-integrated (thermodynamic) properties of the Dyson-inverted propagators. The transformation to a sum over poles is performed introducing n -th order generalized Lorentzians as an improved basis set to represent the spectral function of a propagator, and using analytic expressions to recover the sum-over-poles form. Numerical results for the homogeneous electron gas at the G_0W_0 level are provided to argue for the accuracy and efficiency of such unified approach.

I. INTRODUCTION

Electronic-structure calculations have been and remain a powerful and ever expanding field of research to understand and predict materials properties [1]. The development of methods, algorithms, and hardware brings in continuous progress, allowing for computational materials discovery [2–4], accurate comparison with experiments [5, 6], and even hybrid quantum-computation algorithms [7, 8].

Due to the interaction between the electrons in a system, solving the many-body quantum problem is often at the core of many approaches. Focusing on condensed-matter systems, density-functional theory (DFT) has been one of the most used and successful methods so far [9]. The possibility to map exactly the ground-state solution of the N -body problem to the minimization of a density functional for the energy [10] offers great computational simplifications, allowing the accurate computation of ground-state quantities for most materials. Although mathematically well-defined [11] and computationally inexpensive, it remains challenging to improve the approximate functionals [12, 13] — often resulting in incorrect predictions for complex or strongly-correlated systems [14] — or to address spectroscopic properties [15, 16].

Dynamical (i.e. frequency-dependent) theories like many-body perturbation theory, dynamical mean-field theory, and in general embedding theories offer the flexibility to overcome these limitations of DFT. While the type of embedding differs in different approaches, a common element is the appearance of dynamical potentials.

As an example, many-body perturbation theory (MBPT) reduces the multi-particle electronic degrees of freedom to one via frequency embedding [17]. Dynamical mean-field theory (DMFT) couples a real-space impurity with the rest of the system, requiring self-consistency between the two self-energies acting on the impurity and on the bath [18]. Self-energy-embedding theory (SEET) calculates exactly the frequency-dependent self-energy of strongly-correlated manifolds in solids, and applies it to the remaining weakly interacting orbitals [19, 20]. Coherent electronic-transport theories use a Green's function embedding to calculate the electronic conductance of e.g. a conductor between two semi-infinite leads, coupling the three systems dynamically [21, 22]. Clearly, handling properly frequency-dependent potentials is of central interest in the field.

Using here MBPT as a paradigmatic example, we highlight that the difficulty in treating dynamical quantities has often led to different methodological approaches when calculating spectral or thermodynamic quantities (such as energies, number of particles, chemical potentials). Real-axis calculations are commonly performed to compute the frequency-dependent spectral properties [23–25], while the frequency-integrated thermodynamic properties are typically calculated using an imaginary-axis formalism [26–31]. In a series of papers [32–35] von Barth and coworkers have proposed a formalism partially able to tackle spectra and thermodynamics together for the homogeneous electron gas [36], by modelling the spectral function in frequency-momentum space using Gaussians with k -parametrized centers (quasi-particle energies), broadening (weights), and satellites. Due to its model nature, the approach does not easily offer the flexibility to target realistic systems and in general extend to embedding problems.

Here we introduce a novel approach, termed

* corresponding author: tommaso.chiarotti@epfl.ch

algorithmic-inversion method, applied on sum-over-pole expansions (AIM-SOP), to address the simultaneous calculation of accurate spectral and thermodynamic quantities. Within AIM-SOP, dynamical (frequency-dependent) self-energies are expanded on sum over poles, and the exact solution — at all frequencies — of the Dyson equation is found via a matrix diagonalization. The transformation of a frequency-dependent propagator into a SOP via a representation of its spectral function on a target basis set is greatly improved with the introduction of n -th order generalized Lorentzians as a basis with improved decay properties. The SOP form allows one to compute analytically convolutions and moments of propagators for the calculation of spectral, and thermodynamic properties. Owing to the fulfillment of all sum rules implied by the Dyson equation, we show that the AIM-SOP method becomes essential to have accurate frequency-integrated quantities in a real-axis (thus, spectral oriented) formalism. As a case study, we consider the paradigmatic case of the homogeneous electron gas (HEG), for r_s from 1 to 10, treated at the G_0W_0 level [37–39].

The paper is organized as follows: In Sec. II we introduce the AIM-SOP approach, discussing its main goal and the SOP form for propagators and self-energies. In Sec. II A we provide an overview of the connection between a propagator and its spectral function, first for a continuum and then extending it to treat spectral functions represented on discrete basis sets, as will be used in this work. Then, we consider different basis sets to represent the spectral function and obtain a SOP representation introducing n -th order Lorentzians. In Sec. II B we provide the numerical procedure to transform a propagator sampled on a grid to a SOP representation, and viceversa. In Sec. II C we introduce several useful expressions when dealing with propagators on SOP, such as analytic convolutions and moments, and in Sec. II D we show with a numerical example the representation on SOP for a test propagator. Finally, in Sec. II E we present the algorithmic-inversion method on sum over poles to obtain exact solutions on SOP of any Dyson-like equation. We first provide a mathematical proof for the case of a self-energy on SOP, then we discuss the case of the polarizability inversion, providing a numerical example as proof-of-concept for the procedure. In Sec. III we discuss the application of the method to the test case of the homogeneous electron gas. In Sec. IV we discuss the results obtained applying AIM-SOP to the homogeneous electron gas at the G_0W_0 level, first discussing the $r_s = 4$ case in detail and then presenting results for r_s from 1 to 10. Finally, in Sec. V we draw the conclusions for the paper. Technical aspects of the method are further presented in the Appendices.

II. METHOD: AIM-SOP FOR DYNAMICAL POTENTIALS

In this Section we introduce the algorithmic-inversion method to treat dynamical (frequency-dependent) potentials. The crucial goal for AIM-SOP is to solve exactly and at all frequencies Dyson-like equations for dynamical potential expressed as sum over poles. For this purpose we express frequency-dependent propagators and self-energies (or, say, polarizabilities or screened Coulomb interactions) in a SOP form:

$$G(\omega) = A_0 + \sum_{i=1}^N \frac{A_i}{\omega - z_i}, \quad (1)$$

where the constant term A_0 may be present for self-energies and potentials. Generally, we consider here having complex residues A_i and poles $z_i = \epsilon_i + i\delta_i$ ($\epsilon_i, \delta_i \in \mathbb{R}$). In order to provide the correct analytical structure respecting time-ordering, $\delta_i \geq 0$ when $\epsilon_i \leq \mu$, where μ is the effective chemical potential of the propagator (for a Green's function μ is the Fermi energy of the system, for a polarizability or a screened potential $\mu = 0$).

Throughout this work we will use as case of study the homogeneous electron gas (HEG) also in view of to the extensive algorithmic and numerical results in the literature. In the HEG, due to translational symmetry, the two-point operators (including Green's functions, self-energies, polarizabilities) are diagonal on the plane-wave basis, but the AIM-SOP can be generalized to non-homogeneous systems, as will be discussed in future work.

A. Spectral representations

Following Ref. [33], we consider the spectral representation of a propagator (here the Green's function for simplicity), where G is expressed in terms of its spectral function A ,

$$G(\omega) = \int_{\mathcal{C}} \frac{A(\omega')}{\omega - \omega'} d\omega' \quad (2)$$

by performing a time-ordered Hilbert transform (TOHT), where \mathcal{C} is a time-ordered contour which is shifted above/below the real axis for $\omega' \lesseqgtr \mu$, and where the shift is sent to zero after the integral is computed. Accordingly, the inverse relation to go from G to A is given by:

$$\begin{aligned} A(\omega) &= \frac{1}{2\pi i} [G(\omega) - G^\dagger(\omega)] \operatorname{sgn}(\mu - \omega) \\ &= \frac{1}{\pi} \operatorname{Im} G(\omega) \operatorname{sgn}(\mu - \omega), \end{aligned} \quad (3)$$

the last expression being valid for a scalar Green's function, as is the case for the HEG. Representing the spectral

function on a (finite) basis set $\{b_j(\omega)\}$,

$$A(\omega) = \sum_j a_j b_j(\omega) \operatorname{sgn}(\mu - \epsilon_j) = \sum_j a_j |b_j(\omega)|, \quad (4)$$

with $b_j(\omega)$ centred on ϵ_j and positive (negative) for $\epsilon_j \leq \mu$, respectively, and $a_j > 0$, we also induce a representation of G . This is achieved by introducing a discrete time-ordered Hilbert transform (D-TOHT) as

$$G(\omega) = \sum_j a_j \int \frac{|b_j(\omega')|}{\omega - \omega' - i0^+ \operatorname{sgn}(\epsilon_j)} d\omega', \quad (5)$$

where the sign chosen for b_j in Eq. (4) gives by construction the time-ordered analytic structure of the Green's function. In the case of all $\delta_j \rightarrow 0$ with the number of b_j becoming infinite (continuum representation limit), Eq. (5) becomes the standard TOHT of Eq. (2) (with \mathcal{C} shifted by $\pm i0^+$).

A natural choice is to use a basis of Lorentzian functions centered at different frequencies ϵ_j , according to:

$$|b_j(\omega)| = \mathcal{L}_{\delta_j}(\omega - \epsilon_j) = \frac{1}{\pi} \frac{|\delta_j|}{(\omega - \epsilon_j)^2 + \delta_j^2}, \quad (6)$$

for which the D-TOHT for the single element is analytical, yielding a pole function $1/(\omega - z_j)$ with $z_j = \epsilon_j + i\delta_j$, with the sign convention for δ_j defined as discussed above according to time ordering. Thus, choosing b_j as in Eq. (6) induces a SOP representation for G according to Eq. (1), with $A_i = a_i \in \mathbb{R}$. Once the SOP representation of G is known, i.e. poles and amplitudes are known, the grid evaluation (inverse of the above) is trivial and amounts to performing the finite sum in Eq. (1). This approach ensures a full-frequency treatment of the propagator (approaching the continuum representation limit where Lorentzians becomes delta functions), while preserving an explicit knowledge of the analytical structure and continuation of G .

The main drawback of using Lorentzians to represent G is related to the slowly decaying tails ($1/\omega^2$ for $\omega \rightarrow \infty$) induced in the spectral function when using finite broadening values δ_j . In order to improve on this, we introduce here n -th order generalized Lorentzians to obtain fast-decay basis functions. These are defined as

$$|b_j(\omega)| = \mathcal{L}_{\delta_j}^n(\omega - \epsilon_j) = \frac{1}{N_n \pi} \frac{|\delta_j|^{2n-1}}{(\omega - \epsilon_j)^{2n} + (\delta_j)^{2n}}, \quad (7)$$

where $N_n = [n \sin(\frac{\pi}{2n})]^{-1}$ is the normalization factor (see Appendix A). The D-TOHT of \mathcal{L}_{δ}^n remains analytic and still yields a SOP representation for G (see Appendix A):

$$\int_{\mathcal{C}} d\omega' \frac{\mathcal{L}_{\delta_j}^n(\omega' - \epsilon_j)}{\omega - \omega' - i0^+ \operatorname{sgn}(\epsilon_j)} = \sum_{m=0}^{n-1} \frac{\alpha_m}{\omega - \zeta_{j,m}}, \quad (8)$$

with residues α_m and poles $\zeta_{j,m}$ given by

$$\alpha_m = \frac{1}{i N_n \pi} e^{i \frac{\pi}{2n} (1+2m)} \quad (9)$$

$$\zeta_{j,m} = \epsilon_j + e^{i \frac{\pi}{2n} (1+2m)} \delta_j. \quad (10)$$

Importantly, α_m are complex (and so become the residues $A_i = a_j \alpha_m$ in the SOP representation, i being a combined index). Thus, the spectral function of this SOP has contribution by both the real and the imaginary part of each Lorentzian pole $1/(\omega - \zeta_{j,m})$, resulting in a overall faster decay than each single Lorentzian. Also, it is worth noting that, as for standard Lorentzians, a normalized n -th-order-Lorentzian approaches a Dirac delta for $\delta_j \rightarrow 0^+$. Owing to their fast decay and to this last property, using a SOP for G_0 in term of n -th Lorentzians provides a faster convergence for $\delta \rightarrow 0^+$, in comparison with a SOP representation built on ordinary Lorentzians, as will be also shown later. While the use of n -th order generalized Lorentzians to represent the spectral function $A(\omega)$ provides a faster decay in the imaginary-part of the propagator, it results in a multiplication of the number of poles in the SOP for G (by the degree of the Lorentzian), and in having complex residues. As it will be shown in Sec. II C, the decay properties are fundamental for evaluating the moments of a SOP representation, assuring absolute convergence up to order $2(n-1)$. Also, the use of faster decay basis elements when representing the spectral function improves on the stability of the representation procedure, reducing the off-diagonal elements of the overlap matrix of the basis (see Sec. II B).

Alternatively to n -th order Lorentzians, one could consider e.g. using Gaussian functions to represent $A(\omega)$, and consequently $G(\omega)$, as done in Refs. [32, 33]. Gaussians also allow for an analytical expression of the D-TOHT, at the price, though, of invoking the Dawson [40] or Faddeeva [41] functions to evaluate the real part of the propagator. Because of this, SOP expressions are not available, and basic operations involving propagators (such as those described in Sec. II C) cannot be evaluated analytically and need to be worked out in other ways, e.g. numerically or recasting the expressions in terms of propagator spectral functions [32].

B. Transform to a sum over poles

Once the SOP representation has been introduced, the next important step is to determine numerically the SOP coefficients A_i in Eq. (1), given an evaluation of G on a frequency grid. According to the discussion of Sec. II A, the SOP representation can be seen equivalently as a representation for the Green's function G or for the spectral function A .

As a first case, we consider representing $A(\omega)$ according to Eq. (4), and we do it using the basis of n -th-order generalized Lorentzians introduced in Eq. (7). First, we obtain the coefficients a_j of the representa-

tion by performing a non-negative-least-square (NNLS) fit [41, 42], thus assuring the positivity of all a_j . Then, we use Eqs. (9-10) to get the SOP representation for the propagator. While the position and broadening (ϵ_j, δ_j) of the n -th order Lorentzians could also be optimized by means of a non-linear NNLS fit, here we consider them centred at $\epsilon_j = \frac{1}{2}(\omega_j + \omega_{j-1})$ and broadened with $\delta_j = |\omega_j - \omega_{j-1}|$, and we just linearly optimize a_j . Also, for numerical reasons we prefer to work with the bare imaginary part of G , i.e. without imposing the sign factor of Eq. (3), since this function is smoother than the actual spectral function $A(\omega)$ close to the Fermi level.

Alternatively, one could consider the basis representation induced on G via Eq. (1) in order to directly obtain the A_i and z_i coefficients (residues and poles). As for $A(\omega)$, this can be achieved by a linear or non-linear LS fit (or interpolation) taking advantage of the knowledge of the whole $G(\omega)$ on a frequency grid (and not just of A). Interestingly, the SOP representation in Eq. (1) is a special case of a Padè approximant, written as the ratio of polynomials of order $N - 1$ and N , respectively. Because of this, one can exploit Padè-specific approaches to determine (A_i, z_i) , such as, for instance, Thiele's recursive scheme [43]. We found that this leads to a very efficient method when few tens of poles are considered, becoming numerically unstable beyond. Moreover, since the residues are not constrained to be real and positive (A_i are actually complex), there is no control over the time-ordered position of the poles, and the procedure is non-trivial to extend to the case of n -th order Lorentzians. For the above reasons, in the present work we adopt the first approach, based on the representation of $A(\omega)$.

C. Analytical expressions

Once the SOP representation of a dynamical propagator is available, a number of analytical expressions hold. For instance, the convolution of propagators, such as those involved in the evaluation of the independent-particle polarizabilities in terms of the Green's functions, can be evaluated using Cauchy's residue theorem:

$$\begin{aligned} & \int_{-\infty}^{+\infty} \frac{d\omega'}{2\pi i} G(\omega + \omega') \tilde{G}(\omega') d\omega' = \\ & = \sum_{i,j} \int_{-\infty}^{+\infty} \frac{d\omega'}{2\pi i} \frac{A_i}{\omega + \omega' - z_i} \frac{\tilde{A}_j}{\omega' - \tilde{z}_j} \\ & = \sum_{\substack{i,j \\ \text{Im}\{z_i\} < 0 \\ \text{Im}\{\tilde{z}_j\} > 0}} \frac{A_i \tilde{A}_j}{\omega + \tilde{z}_j - z_i} - \sum_{\substack{i,j \\ \text{Im}\{z_i\} > 0 \\ \text{Im}\{\tilde{z}_j\} < 0}} \frac{A_i \tilde{A}_j}{\omega + \tilde{z}_j - z_i}. \end{aligned} \quad (11)$$

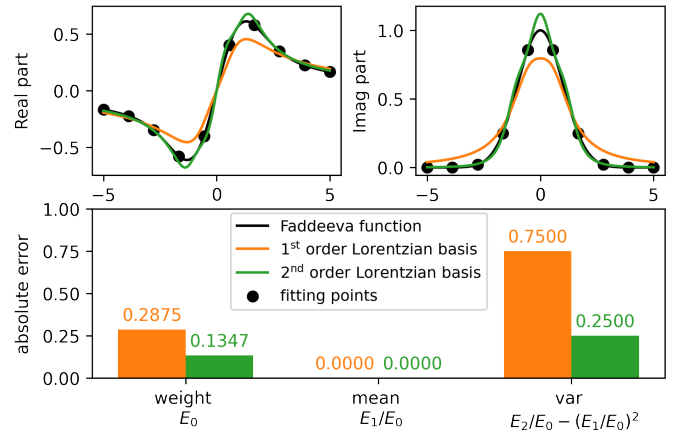


FIG. 1. Numerical example of a transformation to a SOP form. Upper panels: the function to represent is chosen as the Faddeeva function (black line), sampled using only 10 points (black dots). Following the strategy described in Sec. II B, we represent the spectral function of the Faddeeva (a Gaussian) on 1st order (orange) and 2nd order (green) Lorentzians (centred on the midpoint between adjacent grid points, broadened with the size of the interval). The 10 sampled points are fed to the NNLS fit to obtain the coefficients of both the 1st and 2nd Lorentzian basis, and Eqs. (9) and (10) are used to get the SOP. Then, the resulting SOPs are plotted on a fine grid (continuous orange and green lines). Lower panel: absolute error on the computed 0-th to 2nd moments of the SOP representations (obtained in the upper panel) and the analytical Gaussian moments of the Faddeeva function.

Using the the SOP for G , the following integrals can also be computed explicitly:

$$\begin{aligned} E_m[G] &= \int_{-\infty}^{+\infty} \frac{d\omega}{2\pi i} e^{i\omega 0^+} \omega^m G(\omega) \\ &= \sum_{\substack{i \\ \text{Im}\{z_i\} > 0}} A_i z_i^m, \end{aligned} \quad (12)$$

where we refer to the term $E_m[G]$ as the m -th (regularized) moment of G . We restrict the discussion to the first $m = 0$ and $m = 1$ moments, since those are of interest for calculating the number of particles and the total energy in MBPT (see Sec. III B for details). Higher order moments would require a stronger regularization factor in Eq. (12) than $e^{i\omega 0^+}$. We underline that if one uses an n -th-order Lorentzian basis to represent $G(\omega)$ on SOP, the first $2(n - 1)$ moments coincide with the moments of its occupied spectral function $\int_{-\infty}^{\mu} d\omega \omega^{2(n-1)} A(\omega)$. This is shown in Appendix B.

D. Numerical validation

In the following we highlight numerically some properties of the SOP representation. To this aim, we consider a propagator G obtained as the Hilbert transform (HT) of

a Gaussian, analytically expressed via the Faddeeva [41] function (black curves in the top panels of Fig. 1). Here we have assumed the Fermi level to be far enough from the imaginary part of G such that the retarded HT can be used. The objective of the validation is to transform the Faddeeva Green's function sampled on a finite grid to a SOP representation. Following Sec. II B, we represent the Gaussian spectral function on first (ordinary) and second-order Lorentzians, use Eqs. (9) and (10) to get the resulting SOP representation, and then compare the results —orange and green lines for 1st and 2nd order basis, respectively— with the starting Faddeeva Green's function calculated on a much finer grid. We choose to feed the NNLS fitting algorithm with 10 sampling points (for the imaginary part of G) and to use 9 basis functions centered at the midpoints of the grid, and broadened with the width of the interval (in order to ensure an exhaustive cover of the domain). Then we use Eqs. (8-10) to obtain the SOP representation of G (in the case of n th order Lorentzians) from the output of the NNLS procedure.

Underscoring the quality of the representation, the upper panels of Fig. 1 show that using faster-decay 2nd order Lorentzians provides a more accurate result for both the real (left) and imaginary (right) part of G . In the lower panel we also compare the moments of the Faddeeva function with those obtained from Eq. (12) and Eq. (B1). Since absolute convergence for the first and second moments is not ensured for 1st order Lorentzians, meaning that Eq. (B1) does not hold, $E_{n>1}[G]$ has to be calculated according to Eq. (12) and is in general complex. In order to obtain a meaningful result we take its real part, and consider the imaginary one as an error that must be controlled by extending the basis set towards completeness.

E. Algorithmic inversion on SOP

As anticipated in the introduction, within the SOP approach the exact solution at all frequencies of the Dyson equation can be remapped into the diagonalization of a static effective Hamiltonian (Hermitian only under special conditions), a procedure that we refer to as “algorithmic-inversion method on sum over poles” (AIM-SOP); this is a central result for the present work. As mentioned we will use the HEG as a paradigmatic test case, leaving the treatment of the non-homogeneous case to later work. Suppressing then the k momentum index for simplicity, let us suppose to have the SOP representation of the self-energy $\Sigma(\omega)$ and the non-interacting Green's function $G_0(\omega)$ given by

$$\Sigma(\omega) = \sum_{i=1}^N \frac{\Gamma_i}{\omega - \sigma_i}, \quad G_0 = \frac{1}{\omega - \epsilon_0}. \quad (13)$$

Taking advantage of these expressions, the Dyson equation can be rewritten as

$$G(\omega) = [G_0^{-1}(\omega) - \Sigma(\omega)]^{-1} = \frac{1}{\omega - \epsilon_0 - \Sigma(\omega)} = \frac{(\omega - \sigma_1) \cdots (\omega - \sigma_N)}{T_N(\omega)}, \quad (14)$$

in which the $N + 1$ roots of the polynomial

$$T_N(\omega) = (\omega - \epsilon_0) \prod_{i=1, N} (\omega - \sigma_i) - \sum_{j=1, N} \Gamma_j \prod_{\substack{i=1, N \\ i \neq j}} (\omega - \sigma_i) \quad (15)$$

are the $N + 1$ poles of the Green's function (as expected when the self-energy has N poles). Then, the key statement of this Section is that the roots of T_N can be obtained as the eigenvalues of the $(N + 1) \times (N + 1)$ matrix

$$H_{\text{AIM}} = \begin{pmatrix} \epsilon_0 & \sqrt{\Gamma_1} & \cdots & \sqrt{\Gamma_N} \\ \sqrt{\Gamma_1} & \sigma_1 & 0 & 0 \\ \vdots & 0 & \ddots & 0 \\ \sqrt{\Gamma_N} & 0 & \cdots & \sigma_N \end{pmatrix}. \quad (16)$$

We prove this statement by observing that the characteristic polynomial of H_{AIM} is $T_N(\omega)$, and we proceed by induction. Since the $N = 1$ case is trivial we move to the N -th case: using the Laplace expansion on the last line, the characteristic polynomial of the N -th case can be written as

$$p_{H_{\text{AIM}}}(\omega) = \begin{vmatrix} \omega - \epsilon_0 & -\sqrt{\Gamma_1} & \cdots & -\sqrt{\Gamma_N} \\ -\sqrt{\Gamma_1} & \omega - \sigma_1 & 0 & 0 \\ \vdots & 0 & \ddots & 0 \\ -\sqrt{\Gamma_N} & 0 & \cdots & \omega - \sigma_N \end{vmatrix} = (\omega - \sigma_N) T_{N-1}(\omega) + (-1)^N \sqrt{\Gamma_N} \times \begin{vmatrix} -\sqrt{\Gamma_1} & \cdots & -\sqrt{\Gamma_{N-1}} & -\sqrt{\Gamma_N} \\ \omega - \sigma_1 & 0 & 0 & 0 \\ 0 & \ddots & 0 & 0 \\ 0 & \cdots & \omega - \sigma_{N-1} & 0 \end{vmatrix} \quad (17)$$

where we have used the induction hypotheses in the first term of the rhs. Applying the same procedure to the last column of the second term we obtain

$$p_{H_{\text{AIM}}}(\omega) = (\omega - \sigma_N) T_{N-1}(\omega) - \Gamma_N \prod_{i=1, N-1} (\omega - \sigma_i) = T_N(\omega), \quad (18)$$

which completes the proof.

Calling ϵ_i the poles of G we calculate the residues by

equating

$$G(\omega) = \sum_{i=1}^{N+1} \frac{A_i}{\omega - z_i} = \frac{(\omega - \sigma_1) \cdots (\omega - \sigma_N)}{(\omega - z_1) \cdots (\omega - z_{N+1})}, \quad (19)$$

and performing the limit $\lim_{\omega \rightarrow z_i} (\omega - z_i)$ on both sides (Heaviside cover-up method [44]), obtaining:

$$A_i = \frac{\prod_{k=1}^N (z_i - \sigma_k)}{\prod_{j=1, j \neq i}^{N+1} (z_i - z_j)}. \quad (20)$$

We have thus proven that by knowing Σ represented on SOP, the SOP expression of G can be found by the diagonalization of the AIM-SOP matrix H_{AIM} followed by the evaluation of the residues using Eq. (20).

It is worth noting that the H_{AIM} matrix becomes (or can be made) Hermitian under special conditions. This happens when the self-energy residues Γ_i are real and positive, and the self-energy poles have all the same imaginary part $i\delta$, with the usual time-ordered convention according to Eq. (1), also equal to the broadening assumed for the G_0 pole. Then it is possible to include the imaginary part of the poles in the frequency variable ω , and invert $G(\tilde{\omega} \in \gamma)$ on this time-ordered-complex path, in order to have H_{AIM} with only the real part of the poles along the diagonal. Finally, in order to have $G(\omega \in \mathcal{R})$ we analytically continue the solution to the real axis, obtaining $\text{Im}\{\epsilon_i\} = \delta_i$ for the SOP of the Green's function.

We also stress that, given a self-energy represented on SOP, the solution provided by the algorithmic-inversion procedure is exact at all frequencies. This ensures the Green's function fulfills all the sum-rules implied by the Dyson equation, including e.g. the normalization of the spectral weight, and the first and second moments sum rules of the spectral function derived in Ref. [32]. This result is crucial when evaluating frequency-integrated quantities of a Green's function, such as the number of particles or the total energy (see Sec. III B).

Besides the solution of the Dyson equation for G , the AIM-SOP can also be used to solve the Dyson equation for the screened Coulomb interaction $W(\omega)$,

$$\begin{aligned} W(\omega) &= v_c + v_c P(\omega) W(\omega) \\ &= \frac{1}{1 - v_c P(\omega)} v_c = \epsilon^{-1}(\omega) v_c, \end{aligned} \quad (21)$$

i.e. to compute the SOP representation of $W(\omega)$ once a SOP for the irreducible polarizability $P(\omega)$ is provided. Here v_c is the Coulomb potential (recalling that we are suppressing the momentum dependence for simplicity). By letting $P(\omega) = \sum_i \frac{S_i}{\omega - g_i}$, we can write:

$$\begin{aligned} \omega v_c P(\omega) &= \sum_i \omega \frac{v_c S_i}{\omega - g_i} = v_c \sum_i S_i + \sum_i \frac{v_c g_i S_i}{\omega - g_i} \\ &:= c_0 - C(\omega), \end{aligned} \quad (22)$$

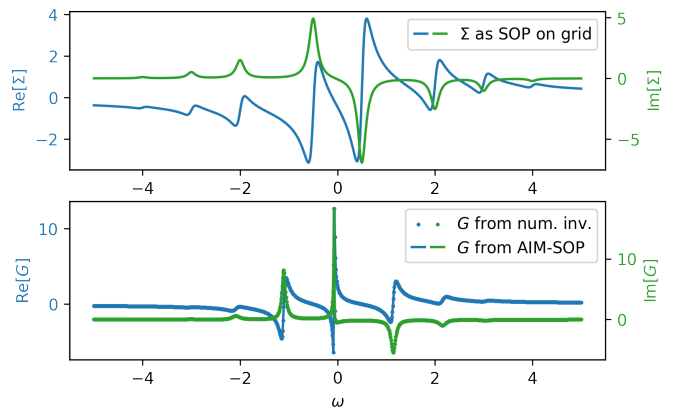


FIG. 2. Numerical example for the algorithmic inversion method on sum over poles. Upper panel: Real (blue) and imaginary (green) part of a time-ordered self-energy, including 8 poles (the occupied pole of G_0 is not shown). Lower panel: Dyson-inverted propagator G obtained with a numerical inversion on a grid (dotted) compared with the SOP representation obtained using AIM-SOP and evaluated on the same grid (solid line). Same color code for real and imaginary parts as in the upper panel.

and following Eq. (21) (multiplied by $\frac{\omega}{\omega}$) we have

$$\epsilon^{-1}(\omega) = \frac{1}{1 - v_c P(\omega)} = \frac{\omega}{\omega - c_0 - C(\omega)}, \quad (23)$$

for which the AIM-SOP matrix can be used to find the poles of $\epsilon^{-1}(\omega)$ and $W(\omega)$. The amplitudes of W are easily found using Eq. (20). Note that by multiplying ϵ^{-1} by $\frac{\omega}{\omega}$ in Eq. (23) we have inserted an extra pole (at $\omega = 0$) which we need to discard from the eigenvalues of the AIM matrix [before applying the residue formula of Eq. (20)], since it simplifies with the ω at the numerator of Eq. (23). Consequently P , ϵ^{-1} , and W all have the same number of poles, at variance with the solution of the Dyson equation for G , where the number of poles of G is increased by one with respect to those of Σ .

As a numerical test for AIM-SOP, we consider the Dyson equation for G within the example of a time-ordered self-energy built with 8 poles, as shown in the upper panel of Fig. 2 (the single pole of G_0 is not reported). In the lower panel we compare the Green's function G obtained from the numerical Dyson inversion on grid — done evaluating Σ on grid, and then inverting — against the Green's function with the algorithmic inversion and evaluated on the frequency grid. The results are identical at the precision of the calculated eigenvalues of the AIM-SOP matrix, since the amplitude calculation of Eq. (20) is typically very well conditioned. Notably, this procedure has been tested in cases where hundreds of poles are used for the self-energy, without any numerical instabilities.

III. APPLICATION: ONE-SHOT G_0W_0 IN THE HEG FROM AIM-SOP

For validation, we apply the AIM-SOP approach to the paradigmatic case of the homogeneous electron gas (HEG), treated at the G_0W_0 level of theory [6, 17, 45]. Since we calculate propagators on the real axis we can easily access spectral (frequency-dependent) properties. The calculation of frequency-integrated ground-state quantities (occupation numbers, total energies, and thermodynamic quantities in general) can be obtained directly from the SOP representation of the spectral quantities computed in the procedure. We stress that usually [26, 46, 47] thermodynamic properties are obtained via additional calculations of propagators (e.g. on the imaginary axis), while in this work spectral properties and integrated quantities are obtained simultaneously using the SOP representation of propagators computed on the real axis.

While some quantities computed using the free-propagator G_0 have known analytical expressions, as is the case for the irreducible polarizability P_0 expressed via the Lindhard function [48, 49], here we recompute explicitly all the propagators needed to evaluate the GW self-energy, making the treatment suitable also for self-consistent calculations. Therefore in the following the only assumption we make is to consider the Green's function as represented on SOP.

A. HEG propagators on the real frequency axis

In order to solve a one-shot G_0W_0 cycle for the spin-unpolarized HEG, we first need to compute the irreducible polarizability at the independent-particle (or RPA) level, according to the integral

$$P(q, \omega) = 2 \int \frac{d\mathbf{k}}{(2\pi)^3} \int \frac{d\omega'}{2\pi i} G(|\mathbf{k} + \mathbf{q}|, \omega + \omega') G(k, \omega'), \quad (24)$$

where $k = |\mathbf{k}|$ and $q = |\mathbf{q}|$ are the moduli of the electron and transferred quasi-momenta, respectively. To compute Eq. (24), the frequency integral (convolution) is performed analytically according to Eq. (11). Then we integrate numerically in spherical coordinates by performing the variable change $x = |\mathbf{k} + \mathbf{q}|$ on the azimuthal angle of \mathbf{k} ,

$$P(q, \omega) = \frac{2}{q(2\pi)^2} \int_0^{+\infty} dk k \int_{|k-q|}^{|k+q|} dx x \times \int \frac{d\omega'}{2\pi i} G(x, \omega + \omega') G(k, \omega'), \quad (25)$$

which allows for the pre-calculation of the analytical convolutions on the two-dimensional (x, k) grid, instead of on the three-dimensional (k, q, θ) space. Exploiting the par-

ity of $P(\omega)$, it is also possible to limit the \mathbf{k} integration to the occupied states (see Appendix C). The numerical integration on the momentum is performed using the trapezoidal rule, which ensures exponential convergence for decaying functions [50].

In order to have a SOP representation for the screened potential W we transform the polarizability calculated on a frequency grid (at fixed momentum q) to a SOP performing a NNLS fitting, following the procedure of Sec. II B. We then solve the Dyson equation using the algorithmic inversion for the polarizability (see Sec. II E) to obtain a SOP for W , and use it for the GW integral. An alternative possibility would be to solve the Dyson equation on a grid (which, due to homogeneity, is an algebraic inversion), and then transform W to a SOP representation. Even admitting for an exact interpolation for the SOP of W on the calculated frequencies (where the Dyson equation is solved on grid), this SOP would suffer from not having solved the Dyson equation for all other frequencies. Very differently, the SOP obtained from the algorithmic inversion provides for an exact solution of the Dyson equation at all frequencies (see Sec. II E). Thus, the sum rules implied by the Dyson equation (moments of the spectral function) are all obeyed by the SOP obtained from the algorithmic inversion, being the exact solution at all frequencies. Conversely, this is not true for the grid inversion where the solution is exact only for isolated frequencies.

Concerning the self-energy integral

$$\Sigma(k, \omega) = \Sigma_x(k) + \frac{1}{(2\pi)^3} \int d\mathbf{q} \times \int_{-\infty}^{+\infty} \frac{d\omega'}{2\pi i} G(|\mathbf{k} + \mathbf{q}|, \omega + \omega') W_{\text{corr}}(q, \omega'), \quad (26)$$

where $W_{\text{corr}} = W - v_c$, we can still use Eq. (11) since we have the SOP representation of W . Again, in Eq. (26) we perform the $x = |\mathbf{k} + \mathbf{q}|$ change of variable obtaining

$$\Sigma(k, \omega) = \Sigma_x(k) + \frac{1}{k(2\pi)^2} \int_0^{+\infty} dq q \int_{|k-q|}^{|k+q|} dx \times \int \frac{d\omega'}{2\pi i} G(x, \omega + \omega') W_{\text{corr}}(q, \omega'), \quad (27)$$

which allows for fewer convolutions (as for the polarizability integral), and use trapezoidal weights as in Eq. (25) for the momentum integration. The solution of the Dyson equation for the Green's function using the algorithmic inversion, and the calculation of frequency-integrated (thermodynamic) quantities, are discussed in the next section.

In Fig. 3 we show the overall flow chart describing the process of going from the knowledge of the initial Green's function to the calculation of the corresponding self-energy (for the HEG in the GW approximation), as implemented in the `heg_sgm.x` program of the AGWX suite [51], by means of the SOP approach. As opposed

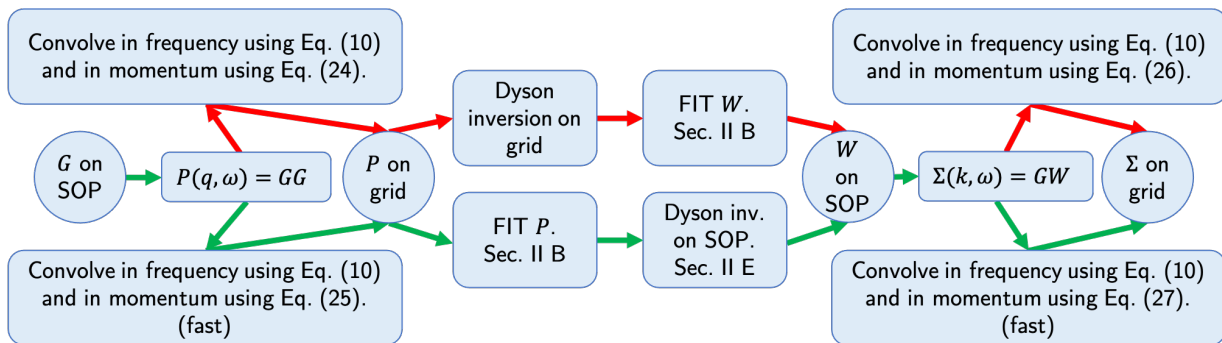


FIG. 3. Flow chart representing different strategies for the calculation of the self-energy given a Green's function G on SOP as input for the `heg_sgm.x` code. The strategy used in this article is highlighted with green lines.

to the path in red, where the Dyson equations are solved on grids, in the green path we highlight the protocol followed in the present work. The crucial difference between the two approaches is the use of the algorithmic-inversion method in order to solve exactly the Dyson equation, providing a SOP for W obeying all sum rules implied by the Dyson equation, as previously discussed in this Section.

B. Frequency-integrated quantities and thermodynamics

Having obtained the self-energy on a frequency grid following the procedure described in Sec. III A, we evaluate the Green's function together with some related frequency-integrated quantities. As mentioned, the SOP approach plays here a central role, enabling the possibility of performing analytical integrals for the moments of G , as those involved in the Galitskii-Migdal expression for the total energy [see Eq. (28) below], and thus to have accurate thermodynamic (frequency-integrated) quantities. Moreover, the use of the algorithmic inversion allows for the exact solution the Dyson equation for the Green's function at all frequencies. The conservation of all sum rules (implied by the Dyson equation, see Sec. II) guaranteed by the AIM-SOP is fundamental when calculating the occupied moments of the spectral function. As an example, the normalization condition of the spectral function is automatically satisfied when G on SOP is obtained using the algorithmic inversion, and allows for not having fitting constrains which would be required, e.g., if we were to use a grid inversion.

In order to exploit the AIM-SOP to get G on a SOP, we obtain the SOP representation of the self-energy by performing a NNLS fitting of $\text{Im}\Sigma(\omega)$ (see Sec. II B). Then, in order to compute the total energy from the knowledge of the Green's function G , we use the Galitski-Migdal

expression [17, 48],

$$\begin{aligned} \frac{E}{V} &= \int \frac{d\mathbf{k}}{(2\pi)^3} \left[\int_{-\infty}^{\mu} d\omega \omega A(k, \omega) + \frac{k^2}{2} \int_{-\infty}^{\mu} d\omega A(k, \omega) \right] \\ &= \int \frac{d\mathbf{k}}{(2\pi)^3} \left[\langle \epsilon_k \rangle + \frac{k^2}{2} n_k \right], \end{aligned} \quad (28)$$

here in Hartree units, where V is the volume of the periodic cell of the electron gas. In this expression, the frequency integrals are performed using the SOP for G , and exploiting Eq. (12) with $m = 1$ and $m = 0$ for the first and second terms, respectively. Here n_k is the k -resolved occupation function, which sums to the total number of particles when integrated over momentum, and $\langle \epsilon_k \rangle$ is the occupied band, i.e. the first momentum of the occupied spectral function. For both $m = 0$ and $m = 1$ moments, the equality between the moments of the Green's function and the moments of the occupied spectral function, Eq. (12) and Eq. (B1), is assured by having used the algorithmic inversion when obtaining the SOP for the Green's function. Indeed, the knowledge of the self-energy on SOP and the use of the algorithmic inversion for solving exactly the Dyson equation ensures that the spectral function

$$A = \frac{1}{\pi} \frac{|\text{Im}\Sigma(\omega)|}{[\omega - \epsilon_0 - \text{Re}\Sigma(\omega)]^2 + [\text{Im}\Sigma(\omega)]^2}, \quad (29)$$

decays at least as $\frac{\text{Im}\Sigma}{\omega^2} = o(\omega^{-3})$, thereby making the first two occupied moments (see Sec. II C) converge.

Similarly to the discussion in Sec. III A, the SOP approach combined with the algorithmic inversion allows one to follow the workflow highlighted by the green path in Fig. 4. Overall, the results presented Sec. IV are obtained using an implementation of the above approach in the `heg_sgm.x` program of the AGWX suite [51].

C. Numerical details

Here we discuss and report the parameters that control the numerical accuracy of the quantities (polariz-

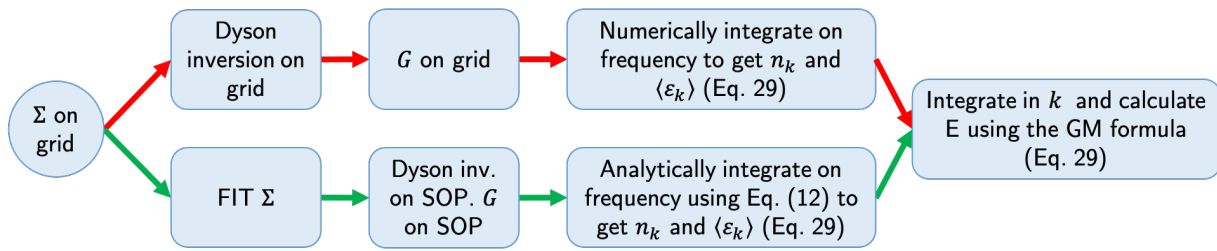


FIG. 4. Flow chart representing different strategies for the calculation of the total-energy given a self-energy Σ , or a spectral function A , on a frequency grid as input for the `heg_sgm.x` code. The strategy used in this article is highlighted with green lines.

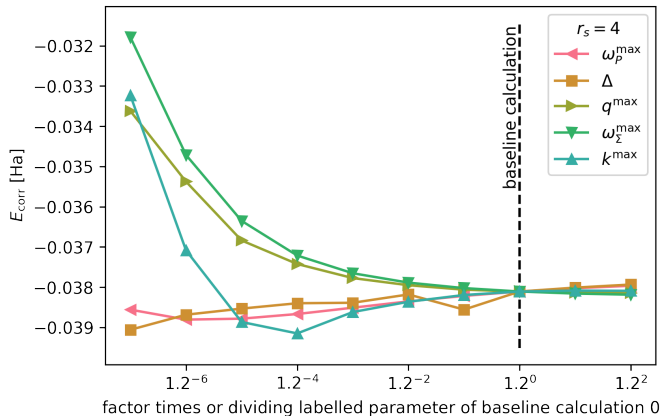


FIG. 5. Convergence study for the correlation energy per particle E_{corr} , obtained with the Galitzki-Migdal formula, and using a Green function from a G_0W_0 calculation for the HEG at $r_s = 4$. The parameters to converge are explained in Sec. III C. We choose to converge E_{corr} for each parameter taking all the others fixed at the converged (second to last point) value. For each different parameter, we increase step-by-step its value by 20% in the convergent direction.

ability, self-energy, total energy) computed by means of Eqs. (25), (27) and (28). In practice, this corresponds to going from left to right in the flow diagram of Fig. 3 following the green path, performing all calculations mentioned in the boxes. The first quantity to be computed is the polarizability $P(q, \omega)$. For each momentum q and frequency ω , we perform the integral of Eq. (25). As k in the integral is limited by k_f (see Sec. III A), the discretization of the k - and x -grids, Δk_P and Δx_P , has to be converged to the zero spacing limit. Also, it is necessary to converge to zero the spacing of the momentum and frequency points of the polarizability- (q, ω) grid, controlled by Δq and $\Delta \omega_P$, along with the grid-upper limits (to infinity) q^{\max} and ω_P^{\max} .

Moving to the central part of the flow chart in Fig. 3, the SOP representation of the polarizability is obtained following the method of Sec. II B, and placing the center of the 2nd order Lorentzians on the mid points of the frequency grid, which improves the accuracy of the fit as $\Delta \omega_P \rightarrow 0$. Next, we employ the algorithmic-inversion method to go from the SOP representation of the po-

larizability to the SOP of the screened-potential W (exact to machine precision, see Sec. II E). Using the SOP representation of W (and of G), the self-energy integral (right part of Fig. 3), Eq. (27), is formally identical to the integral in Eq. (25) for the polarizability. Therefore, the remaining parameters to converge are Δx_Σ , Δk , $\Delta \omega_\Sigma$, k^{\max} , and ω_Σ^{\max} (using the same notation adopted above). As for the screened-potential W , we obtain the SOP representation of the self-energy following Sec. II B, and placing 2nd-order Lorentzians on the mid points of the frequency grid. Finally, we obtain the SOP representation of the Green's function employing the algorithmic-inversion method.

In principle, for each computed quantity which depends on the Green's function G , e.g. via the spectral function or its integrals, we should study the numerical stability of the computational procedure with respect to all the above parameters. Our numerical approach allows for the evaluation of the Green's function and the related spectral quantities on the real-axis, which are then used for the computation of thermodynamic quantities. In this work, we choose to converge the total energy (as obtained in Sec. III C), which is sensitive enough to guarantee a reasonable convergence for the other (spectral) properties of interest here. By changing individually each parameter (increase or decrease by 20% of its value towards convergence), we study the stability of the total energy against the selected parameter, keeping the values of all the others fixed at a reference point (baseline calculation of Fig. 5). Each target parameter is then converged separately until a plateau for the subsequent values of the computed quantity is observed. We evaluate the error on the result considering the two most distant values among those in the plateau.

Importantly, it is possible to reduce the number of parameters to converge from 13 to 5, by linking all the grid-spacing and broadening parameters together into a single variable, Δ , which ensures convergence for $\Delta \rightarrow 0^+$. Specifically, we bind those parameters together by setting $\Delta = \Delta k_P = 5\Delta x_P = \frac{1}{6}\Delta \omega_W = \frac{1}{9}\Delta q = \frac{1}{25}\Delta \omega_\Sigma = \Delta x_\Sigma = \frac{1}{3}\Delta k_\Sigma = \frac{5}{4}\delta_P = \frac{1}{100}\delta_\Sigma$. Together with Δ , the grid-limit parameters are converged separately, following the strategy designed above. The converged values obtained for all the calculated densities are: $\Delta = 0.004 k_f$,

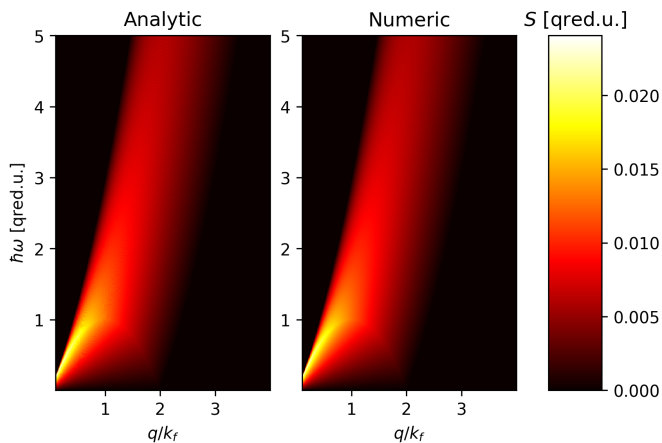


FIG. 6. Spectral part of the polarizability of the HEG at $r_s = 4$ in a one-shot G_0W_0 calculation. Energy units are q -reduced: $E/(\epsilon_f f(q/k_f))$ with $f(x) = x(1/\sqrt{x} + x)$ and k_f the Fermi momentum. Left panel: data calculated with Eq. (25), represented in SOP, and then evaluated on a frequency grid. Right panel: Analytic results [52] on the same frequency-momentum grid.

$$q^{\max} = 7.292 k_f, k^{\max} = 3.60 k_f, \omega_P^{\max} = 5.0 \epsilon_f, \omega_\Sigma^{\max} = 10.985 \epsilon_f, \text{ where } k_f \text{ is the Fermi momentum and } \epsilon_f \text{ the Fermi energy.}$$

IV. RESULTS

In this Section we discuss the results obtained applying the SOP approach to the case of the one-shot G_0W_0 calculation in the HEG. First we extensively discuss the $r_s = 4$ case, also one of the most studied in the literature, then in Sec. IV C we provide the results for densities ranging from $r_s = 1$ to $r_s = 10$.

A. Spectral propagators on the real axis

We start by considering the independent particle polarizability $P_0(q, \omega)$ computed at the G_0 level. In Fig. 6 we compare the imaginary part of P_0 , calculated using Eq. (25) and represented on SOP (fitted to 2nd order Lorentzians with NNLS and then evaluated on a frequency grid, see Secs. II B and II D), with its analytic expression [52] (note that this is the only analytic result we use as a check – all others are evaluated numerically). The $\delta \rightarrow 0^+$ broadening used in G_0 in order to converge the momentum integration does not sensibly affect the calculations. It is worth noting that the use of 2nd order Lorentzians with respect to simple Lorentzians eases this convergence, providing for the same δ and k -grid spacing better agreement with the analytic result at $\delta = 0$ (thermodynamic limit, see Sec. II A). From the plot comparison we can qualitatively infer that the SOP approach, together with its numerical implementation, is working

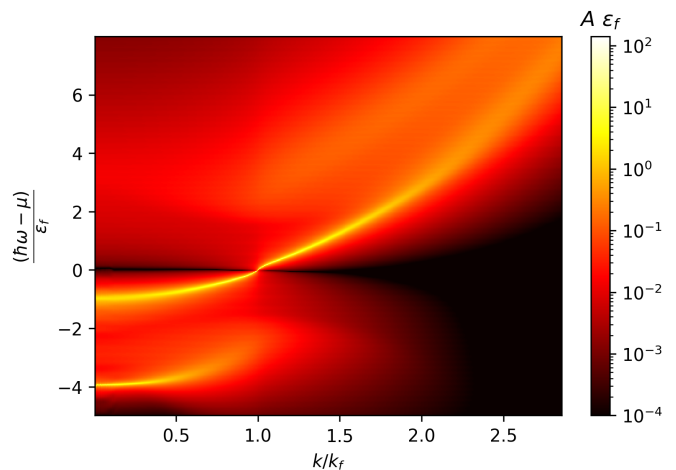


FIG. 7. Spectral function of the HEG at $r_s = 4$ from a G_0W_0 calculation. The Fermi energy is $\epsilon_f = \frac{\hbar^2 k_f^2}{2m_e}$ with k_f the Fermi momentum. $\mu = \epsilon_f + \text{Re}\Sigma(k_f, \epsilon_f) = \epsilon_f(1 - 0.0545)$ is the chemical potential. The scale of the color-map is logarithmic.

effectively in computing and representing the dynamical polarizability across a range of different values of q .

Next, we look at the self-energy numerical procedures by examining directly the G_0W_0 spectral function as shown in Fig. 7. This is obtained evaluating Eq. (27), representing the self-energy on SOP with 2nd order Lorentzians, using the algorithmic inversion for the self-energy, and then evaluating the Green's function on a frequency grid. Focusing the attention on the lower satellite as well as on the quasi-particle band, we can see that Fig. 7 compares well with [30, 53] (note that, at variance with [30], we use a logarithmic scale to represent the intensity of the spectral function, in order to highlight its structure). The plasmaron peak [53] is very visible for small momenta where the quasi-particle band broadens, while the satellite band in the occupied-frequency range ($\omega < \mu$) is sharper. As k approaches k_f , the plasmaron disappears and the quasi-particle band becomes more peaked. At $k = k_f$ the spectral function presents the typical metallic divergence along the quasi-particle band, and occupied and empty satellites are almost of the same weight, in agreement with Ref. [32]. For $k > k_f$ satellites coming from empty states ($\omega > \mu$) become dominant along with the quasi-particle band, and no structure resembling a plasmaron hole appears.

B. Frequency integrated quantities and thermodynamics

We now study convergence and stability of the total energies. Following the prescription of Sec. III, we use the spectral function on SOP obtained in Sec. IV A, Eq. (12) to get analytically the occupation number n_k and the occupied-band energy ϵ_k (see Sec. III B), and finally numerically integrate the momenta of Eq. (28) to obtain the

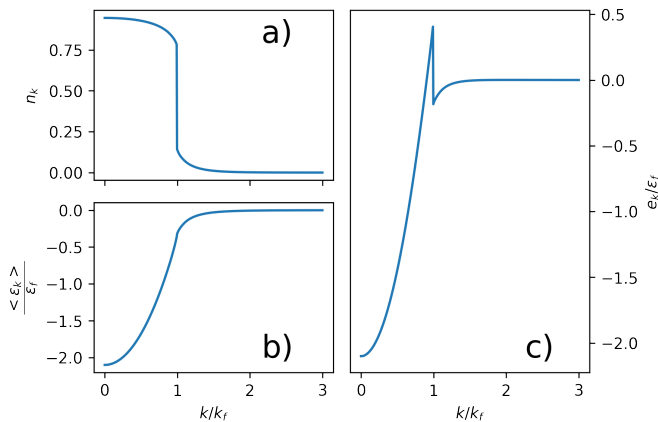


FIG. 8. Selected frequency integrated quantities from a G_0W_0 calculation of the HEG at $r_s = 4$. In panel a) the occupation number in arbitrary units, and in panel b) the occupied band ($\langle \epsilon_k \rangle$) (see Sec. III B for details), both as functions of the momentum k . In panel c) the Galitzki-Migdal total-energy resolved over k -contributions e_k , according to the rhs of Eq. (28) as function of the momentum k . k_f and ϵ_f are the Fermi momentum and energy respectively.

total energy. To perform the convergence study on the total energy, we follow the approach described in Sec. III C which consists in converging all parameters for the calculation separately. Being the HEG a metal, the use of the algorithmic-inversion method to get a spectral function that obeys all sum rules (implied by the Dyson equation, see Sec. II E for details), including the normalization condition for the spectral function, is crucial for obtaining well-converged results. Indeed, the Luttinger discontinuity of n_k makes the value of the total energy from the Galitzki-Migdal very sensitive to the converging parameters.

In Fig. 5 we show the convergence study for the correlation energy per particle (total energy minus Fock-exchange): the convergence value for $r_s = 4$ is 0.0381 ± 0.0003 Ha in agreement with Refs. [26] (with a difference of 0.0003 Ha), where calculations were done along the imaginary axis. In panel a) of Fig. 8 we plot n_k , and in panel b) $\langle \epsilon_k \rangle$ (as defined in Sec. III B). The occupation number n_k presents a sharp Luttinger discontinuity, which indicates that the broadening used in Eq. (27) is well-controlled and does not spoil the quality of the results. In panel c) of Fig. 8 we plot the total-energy resolved over k -contributions e_k [rhs of Eq. (28)]. As previously mentioned, due to the presence of the Luttinger discontinuity, this function is sharp and thus difficult to integrate, at variance, e.g. with the RPA-Klein-energy functional, which is expected to be smoother [54].

G_0W_0 HEG Correlation Energies $ E_{\text{corr}} $			
r_s	This work	Ref. [35]	Ref. [26]
1	0.0749 (± 0.0015)	0.0722	0.0690
2	0.0545 (± 0.0003)	0.0539	0.0530
3	0.0451 (± 0.0008)	0.0448	-
4	0.0381 (± 0.0003)	0.0382	0.0378
5	0.0333 (± 0.0002)	0.0355	0.0331
6	0.0297 (± 0.0002)	-	-
7	0.0268 (± 0.0002)	-	-
8	0.0245 (± 0.0002)	-	-
9	0.0226 (± 0.0002)	-	-
10	0.0210 (± 0.0002)	-	0.0207

TABLE I. Correlation energies as function of r_s for the HEG at the G_0W_0 level. Energies are in Hartree units.

γ	β_1	β_2
-0.1929	1.1182	0.4609
Covariance matrix of the fit		
0.00022	-0.00277	-0.00011
	0.03497	0.00123
		0.00014

TABLE II. Parameters of the correlation energy fit in Hartree, Eq. (30) (same functional form as in [55]), using the data of Table I, and the covariance matrix of the fit. The fitted function is plotted in Fig. 11.

C. G_0W_0 for a broad range of HEG densities

In this Section we report results for the HEG with r_s ranging from 1 to 10 studied at the G_0W_0 level, following the same approach used for $r_s = 4$. In Fig. 9 we show the computed data for the spectral function obtained with the AIM-SOP approach. In the chosen units (ϵ_f for the energy and k_f for the momentum) the spectral function for increasing r_s shows an increase in the separation between the quasi-particle band and the satellite occupied and empty bands. Indeed, in these units r_s controls the interaction strength—see Eq. (3.24) of Ref. [52]—with the limits of the non-interacting gas obtained for $r_s \rightarrow 0$ and the strongly interacting gas corresponding to $r_s \rightarrow \infty$. Accordingly, the plasmaron peak of the satellite band at small momenta is weakened for smaller r_s . The same behaviours can be observed for the occupation factor of Fig. 10 for the different densities. For $r_s \rightarrow 0$ the HEG approaches the non-interacting limit and the occupation number drops from 1 to 0 for increasing k/k_f . Going toward $r_s = 10$ the jump becomes smaller, since the quasi-particle is reduced due to the more evident satellite bands, as it can be seen from Fig. 9.

In Table I we report the corresponding total energies computed at the different densities, together with the available (to our knowledge) results in the literature.

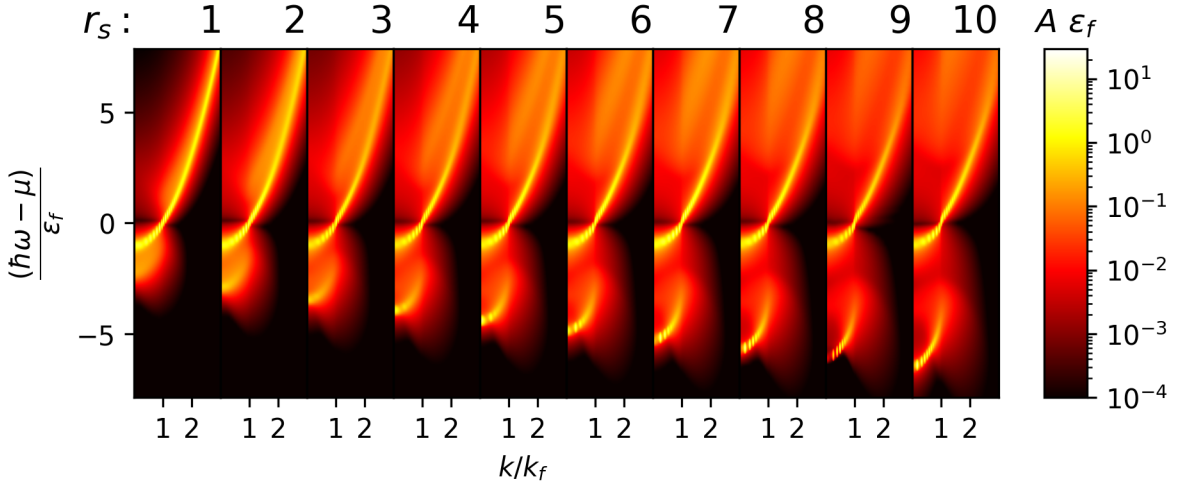


FIG. 9. Spectral functions of the HEG at several densities. At the top r_s specifies the density. The Fermi energy is $\epsilon_f = \frac{\hbar^2 k_f^2}{2m_e}$ with k_f the Fermi momentum. $\mu = \epsilon_f + \text{Re}\Sigma(k_f, \epsilon_f)$ is the chemical potential. The color map is logarithmic.

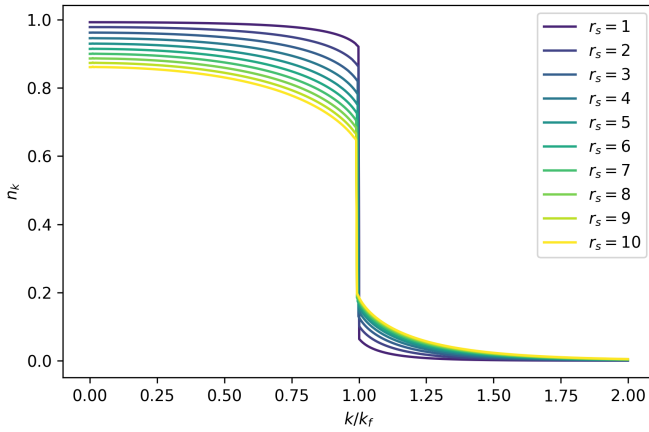


FIG. 10. Occupation factor in arbitrary units for several densities (r_s from 1 to 10). k_f is the Fermi momentum.

Since the calculations of Ref. [26] were done on the imaginary axis, we shall consider those as the most accurate for the comparison. We refer to the Supplemental Material [57] for the convergence studies of the total energies for the different densities. We find at $r_s = 1$ the largest discrepancy (0.0059 Ha) with respect to the data of Ref. [26]. This can be rationalized by noting, e.g., that n_k is a steeper function, thereby enhancing the numerical issues of the Galitzki-Migdal expression discussed in Sec. III B. To deepen the understanding of this numerical discrepancy, aside the convergence study of Fig. 1 provided in the Supplemental Material [57], we performed an additional calculation increasing the refinement parameter Δ by 20%, aiming at increasing the accuracy in the integral grids, to target the steeper character of $r_s = 1$. The result, 0.0736 Ha against 0.0749 Ha of Table I, is acceptable considering the error of 0.0015 Ha of Table I. Most importantly we stress that at variance

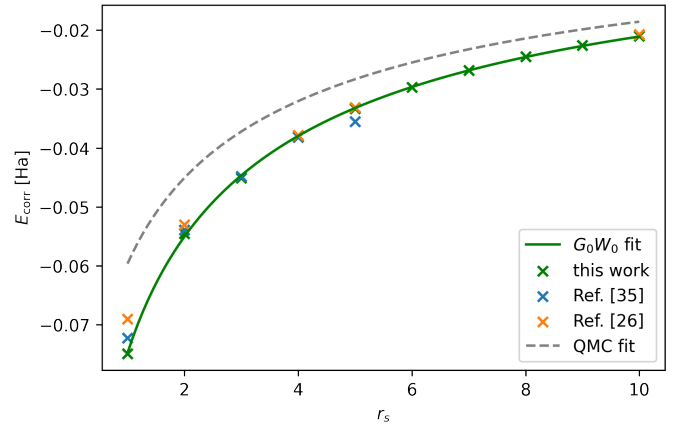


FIG. 11. Correlation energy in Hartree units for several densities within the G_0W_0 approximation in the HEG. In green we show the results found in this work (see Sec. IV C) compared with those found in [35] in blue, and with [26] in orange. In green we plot the correlation energy fit of Eq. (30) (same functional form as in [55]) on the present (green) data. For reference, in dashed grey we add also the Quantum Monte Carlo data obtained by Ceperley and Alder [56] in the fit made by Perdew and Zunger [55].

with Ref. [26], our procedure provides not only accurate frequency-integrated quantities (e.g. the total energy), but also precise spectral properties on the real axis (key quantities for spectroscopy).

In Fig. 11 we plot the correlation energy of Table I as a function of r_s , including the Perdew-Zunger (PZ) fit of the Quantum Monte Carlo (QMC) Ceperley Alder data as a reference [55, 56]. We also exploit the same functional form of PZ to fit our data, providing in Table II γ , β_1 , and β_2 for the fitting function for the correlation energy

of the HEG (in Hartree):

$$E_{\text{corr}}(r_s) = \frac{\gamma}{1 + \beta_1 \sqrt{r_s} + \beta_2 r_s}, \quad (30)$$

together with the covariance matrix of the fit. In Fig. 11 we plot the result of the fit as a green line.

V. CONCLUSIONS

In this work we introduce the novel algorithmic-inversion method on sum over poles (AIM-SOP) to handle frequency-dependent quantities in dynamical theories. Specializing to the case of many-body perturbation theory, we show that the AIM-SOP is able to provide a unified formalism for spectral and thermodynamic properties of an interacting-electron system. Expanding all frequency-dependent quantities on SOP, we use AIM-SOP to solve exactly and at all frequencies Dyson-like equations, getting analytic frequency-dependent (spectral) and frequency-integrated (thermodynamic) properties. This is allowed by the mapping of the Dyson equation to an effective Hamiltonian of dimension controlled by the number of poles in the SOP of the self-energy (see Sec. II E). The transformation of frequency-dependent quantities into SOP is performed exploiting the representation of their spectral functions on different basis sets: aside from the standard choice of a basis of Lorentzians, we introduce n -th order generalized Lorentzian basis elements (see Sec. II A) with improved decay properties. This allows for better numerical stability when transforming a propagator to SOP (see Sec. II B), improved analytic properties for calculating the thermodynamic quantities (see Sec. II C), and an acceleration of convergence to the thermodynamic limit (zero broadening and infinite k -space sampling). Also, once the SOP representation of a propagator is known, we use the Cauchy residue theorem to calculate convolutions and (occupied) moments, accessing both spectral and thermodynamic quantities (see Sec. II C).

In order to have a working example of the AIM-SOP approach, we apply it to the paradigmatic case of many-body perturbation theory at the G_0W_0 level for the HEG at several densities (r_s from 1 to 10). Using AIM-SOP, we are able to provide accurate spectra simultaneously with precise frequency-integrated quantities (e.g. occupation numbers and total energies). At the available densities, we find very good agreement with Refs. [30, 53] for the spectral function. Moving to the total energy, we provide an in depth study of the stability and convergence of our results, finding quantitative agreement with Ref. [26] for the available r_s , where calculations are performed on the imaginary axis.

Although in this article we study a homogeneous system as test case, the AIM-SOP approach aims to treat realistic non-homogeneous systems in the more general framework of dynamical embedding theories, for a full-

frequency representation of potentials and propagators, the flexibility for self-consistent calculations, and the exact solution of Dyson-like equations.

VI. ACKNOWLEDGMENTS

This work was supported by the Swiss National Science Foundation (SNSF) through grant No. 200021-179138 (T.C.) and its National Centre of Competence in Research MARVEL on ‘Computational Design and Discovery of Novel Materials’ (N.M.), and from the EU Commission for the MaX Centre of Excellence on ‘Materials Design at the eXascale’ under grant no. 824143 (N.M., A.F.).

Appendix A: Sum-over-poles representation of an n -th order Lorentzian

In this Appendix we obtain the SOP representation of a Green’s function from an n -th order Lorentzian spectral function. Recalling Sec. II A, the discrete time-ordered Hilbert transform (Eq. (5)) of a (not normalized) n -th order Lorentzian,

$$\int \frac{d\omega'}{\pi} \frac{1}{\omega - \omega' - i0^+ \text{sgn}(\epsilon_j)} \frac{|\delta_j|^{2n-1}}{(\omega' - \epsilon_j)^{2n} + (\delta_j)^{2n}}, \quad (A1)$$

induces a SOP representation for the Green’s function, see Sec. II A. The expression in Eq. A1 can be computed using the residue theorem. Closing the contour in the upper/lower plane for $\omega \lesseqgtr \mu$, the poles of the integrand $\zeta_{j,m} = \epsilon_j + e^{i\frac{\pi}{2n}(1+2m)}\delta_j$ come only from the spectral function A . Using L’Hôpital’s rule, the residues of the integrand are reduced to

$$R_{j,m} = -\frac{1}{2n\pi} \frac{e^{i\frac{\pi}{2n}(1+2m)}}{\omega - \zeta_{j,m} - i0^+ \text{sgn}(\epsilon_j)}. \quad (A2)$$

Thus, taking the limit for \mathcal{C} on the real-axis, poles and residues of the SOP for G are those in Eqs. (10) and (9). The normalization of the n -th order Lorentzian is given by summing α_m of Eq. (9) and using the geometric sum,

$$N_n = -\frac{i}{n} \sum_{m=0}^{n-1} e^{i\frac{\pi}{2n}(1+2m)} = \frac{1}{n \sin\left(\frac{\pi}{2n}\right)}. \quad (A3)$$

Appendix B: Moments of a propagator and occupied moments of its spectral function

In this Section we discuss the equality between the (regularized) moments of a propagator Eq. (12) and the occupied moments of its spectral function. For simplicity of notation we restrict to the case of a single n -th Lorentzian \mathcal{L}_δ^n , as defined in Eq. (7), and focus on the $m = 2(n-1)$ case [again here we suppose the integral in

Eq. (12) converges which is assured by $m = 0$ and $m = 1$, but must be stronger regularized for higher degrees]:

$$\begin{aligned} E_{2(n-1)}[G] &= \int_{-\infty}^{+\infty} \frac{d\omega}{2\pi i} \int d\omega' \frac{e^{i\omega 0^+} \omega^{2(n-1)}}{\omega - \omega'} \mathcal{L}_{\delta_j}(\omega' - \epsilon_j) \\ &= \int_{-\infty}^{\mu} d\omega' e^{i\omega' 0^+} (\omega')^{2(n-1)} \mathcal{L}_{\delta_j}(\omega' - \epsilon_j) \\ &= \int_{-\infty}^{\mu} d\omega \omega^{2(n-1)} A(\omega) \end{aligned} \quad (\text{B1})$$

where $A(\omega)$ is the spectral function of G . To go from the second to the third line, we used the $1/\omega^{2n}$ decay of the n -th Lorentzian, and applied the dominated convergence theorem which allows for the 0^+ limit to be performed inside the integral. The same derivation holds for lower degree moments. For the higher order moments, $m > 2(n-1)$ it is not possible to discard the $e^{i\omega 0^+}$ factor in the integral, thus $E_{m>2(n-1)}[G]$ becomes complex. The equality between $E_{m>2(n-1)}[G]$ [first and second line of Eq. (B1)] and the occupied moments of A [third line of (B1)] is lost, with the integral for the occupied moments of A diverging. The divergence happens because we cannot exchange the limit of the finite representation (controlled by δ_i) and the lower bound $a \rightarrow -\infty$ of the integral $\int_a^{\mu} d\omega \omega^{2(n-1)} A(\omega)$. Numerically, this translates into performing the two limits in order, i.e. fixing the lower bound of the integral and controlling the integral stability for $\delta_i \rightarrow 0$, then lower a and again convergence the result for $\delta_i \rightarrow 0$, and repeat until both convergences are achieved. In this continuous limit for the representation of A the integral for the occupied moments of A [third line of Eq. (B1)] coincides with $E_m[G]$ [last line of Eq. (12)], thus the equality between the two is recovered.

Appendix C: Exploiting parity of the RPA-polarizability integral

In this Appendix we show how it is possible to exploit the parity of the polarizability $P(q, \omega)$ at fixed momentum \mathbf{q} . As explained in Sec. II C, the SOP approach allows to compute analytically the convolution of Eq. (24). Using Eq. (11) in Eq. (24), the polarizability may be rewritten as

$$\begin{aligned} P(q, \omega) &= 2 \int \frac{d\mathbf{k}}{(2\pi)^3} \times \\ &\left[\sum_{\substack{i,j \\ \text{Im}\{z_i(|\mathbf{k}+\mathbf{q}|)\} < 0 \\ \text{Im}\{z_j(k)\} > 0}} \frac{A_i(|\mathbf{k}+\mathbf{q}|)A_j(k)}{\omega + z_j(k) - z_i(|\mathbf{k}+\mathbf{q}|)} \right. \\ &\left. - \sum_{\substack{i,j \\ \text{Im}\{z_i(|\mathbf{k}+\mathbf{q}|)\} > 0 \\ \text{Im}\{z_j(k)\} < 0}} \frac{A_i(|\mathbf{k}+\mathbf{q}|)A_j(k)}{\omega + z_j(k) - z_i(|\mathbf{k}+\mathbf{q}|)} \right], \end{aligned} \quad (\text{C1})$$

where we did not yet restrict to the G_0 case in which only one pole is present. Calling $I(|\mathbf{k}+\mathbf{q}|_{\text{unocc}}, k_{\text{occ}}, \omega)$ the first term in the rhs (k_{occ} labels the occupied states with momentum k , while $|\mathbf{k}+\mathbf{q}|_{\text{unocc}}$ refers to empty states), and setting $\mathbf{k}+\mathbf{q} \rightarrow -\mathbf{k}$ in the second term,

$$\begin{aligned} P(q, \omega) &= 2 \int \frac{d\mathbf{k}}{(2\pi)^3} \left[I(|\mathbf{k}+\mathbf{q}|_{\text{unocc}}, k_{\text{occ}}, \omega) \right. \\ &\left. + I(|\mathbf{k}+\mathbf{q}|_{\text{unocc}}, k_{\text{occ}}, -\omega) \right], \end{aligned} \quad (\text{C2})$$

it is possible limit the calculation to the first term. For the case of $G = G_0$ of Sec. III A, the occupied states at momentum k are all within the Fermi sphere, and thus we can limit the momentum integration to the sphere of radius k_f , i.e. $k \leq k_f$ in Eqs. (24) and (25).

-
- [1] N. Marzari, A. Ferretti, and C. Wolverton, *Electronic-structure methods for materials design*, Nature Materials **20**, 736 (2021).
- [2] J. Hafner, C. Wolverton, and G. Ceder, *Toward Computational Materials Design: The Impact of Density Functional Theory on Materials Research*, MRS Bulletin **31**, 659 (2006).
- [3] S. Curtarolo, G. L. W. Hart, M. B. Nardelli, N. Mingo, S. Sanvito, and O. Levy, *The high-throughput highway to computational materials design*, Nature Materials **12**, 191 (2013).
- [4] N. Mounet, M. Gibertini, P. Schwaller, D. Campi, A. Merkys, A. Marrazzo, T. Sohier, I. E. Castelli, A. Cepellotti, G. Pizzi, and N. Marzari, *Two-dimensional materials from high-throughput computational exfoliation of experimentally known compounds*, Nature Nanotechnology **13**, 246 (2018).
- [5] J. S. Zhou, L. Reining, A. Nicolaou, A. Bendounan, K. Ruotsalainen, M. Vanzini, J. J. Kas, J. J. Rehr, M. Muntwiler, V. N. Strocov, F. Sirotti, and M. Gatti, *Unraveling intrinsic correlation effects with angle-resolved photoemission spectroscopy*, Proceedings of the National Academy of Sciences **117**, 28596 (2020).
- [6] L. Reining, *The GW approximation: content, successes and limitations*, Wiley Interdisciplinary Reviews: Computational Molecular Science **8**, e1344 (2018).
- [7] H. Ma, M. Govoni, and G. Galli, *Quantum simulations of materials on near-term quantum computers*, npj Computational Materials **6**, 1 (2020).
- [8] H. Ma, N. Sheng, M. Govoni, and G. Galli, *Quantum Embedding Theory for Strongly Correlated States in Materials*, Journal of Chemical Theory and Computation **17**, 2116 (2021).
- [9] R. Van Noorden, B. Maher, and R. Nuzzo, *The top 100 papers*, Nature News **514**, 550 (2014).
- [10] P. Hohenberg and W. Kohn, *Inhomogeneous Electron Gas*, Physical Review **136**, B864 (1964).

- [11] M. Levy, *Universal variational functionals of electron densities, first-order density matrices, and natural spin-orbitals and solution of the v -representability problem*, Proceedings of the National Academy of Sciences **76**, 6062 (1979).
- [12] J. P. Perdew, K. Burke, and M. Ernzerhof, *Generalized Gradient Approximation Made Simple*, Physical Review Letters **77**, 3865 (1996).
- [13] J. Sun, A. Ruzsinszky, and J. Perdew, *Strongly Constrained and Appropriately Normed Semilocal Density Functional*, Physical Review Letters **115**, 036402 (2015).
- [14] A. J. Cohen, P. Mori-Sánchez, and W. Yang, *Insights into Current Limitations of Density Functional Theory*, Science **321**, 792 (2008).
- [15] J. P. Perdew, W. Yang, K. Burke, Z. Yang, E. K. U. Gross, M. Scheffler, G. E. Scuseria, T. M. Henderson, I. Y. Zhang, A. Ruzsinszky, H. Peng, J. Sun, E. Trushin, and A. Görling, *Understanding band gaps of solids in generalized Kohn–Sham theory*, Proceedings of the National Academy of Sciences **114**, 2801 (2017).
- [16] N. L. Nguyen, N. Colonna, A. Ferretti, and N. Marzari, *Koopmans-Compliant Spectral Functionals for Extended Systems*, Physical Review X **8**, 021051 (2018).
- [17] R. M. Martin, L. Reining, and D. Ceperley, *Interacting Electrons Theory and Computational Approaches*, Cambridge University Press, 2016.
- [18] A. Georges, G. Kotliar, W. Krauth, and M. J. Rozenberg, *Dynamical mean-field theory of strongly correlated fermion systems and the limit of infinite dimensions*, Reviews of Modern Physics **68**, 13 (1996).
- [19] A. A. Kananenka, E. Gull, and D. Zgid, *Systematically improvable multiscale solver for correlated electron systems*, Physical Review B **91**, 121111 (2015).
- [20] T. N. Lan and D. Zgid, *Generalized Self-Energy Embedding Theory*, The Journal of Physical Chemistry Letters **8**, 2200 (2017).
- [21] A. Calzolari, N. Marzari, I. Souza, and M. Buongiorno Nardelli, *Ab initio transport properties of nanostructures from maximally localized Wannier functions*, Physical Review B **69**, 035108 (2004).
- [22] A. Ferretti, A. Calzolari, B. Bonferroni, and R. D. Felice, *Maximally localized Wannier functions constructed from projector-augmented waves or ultrasoft pseudopotentials*, Journal of Physics: Condensed Matter **19**, 036215 (2007).
- [23] L. Hedin, J. Michiels, and J. Inglesfield, *Transition from the adiabatic to the sudden limit in core-electron photoemission*, Physical Review B **58**, 15565 (1998).
- [24] A. Damascelli, Z. Hussain, and Z.-X. Shen, *Angle-resolved photoemission studies of the cuprate superconductors*, Reviews of Modern Physics **75**, 473 (2003).
- [25] D. Golze, M. Dvorak, and P. Rinke, *The GW Compendium: A Practical Guide to Theoretical Photoemission Spectroscopy*, Frontiers in Chemistry **7** (2019).
- [26] P. García-González and R. W. Godby, *Self-consistent calculation of total energies of the electron gas using many-body perturbation theory*, Physical Review B **63**, 075112 (2001).
- [27] A. Schindlmayr, P. García-González, and R. W. Godby, *Diagrammatic self-energy approximations and the total particle number*, Physical Review B **64**, 235106 (2001).
- [28] N. E. Dahlen and U. v. Barth, *Variational energy functionals tested on atoms*, Physical Review B **69**, 195102 (2004).
- [29] N. E. Dahlen, R. van Leeuwen, and U. von Barth, *Variational energy functionals of the Green function and of the density tested on molecules*, Physical Review A **73**, 012511 (2006).
- [30] Y. Pavlyukh, G. Stefanucci, and R. van Leeuwen, *Dynamically screened vertex correction to GW*, Physical Review B **102**, 045121 (2020).
- [31] A. L. Kutepov, *Electronic structure of Na, K, Si, and LiF from self-consistent solution of Hedin’s equations including vertex corrections*, Physical Review B **94**, 155101 (2016).
- [32] U. von Barth and B. Holm, *Self-consistent GW results for the electron gas: Fixed screened potential W within the random-phase approximation*, Physical Review B **54**, 8411 (1996).
- [33] B. Holm and F. Aryasetiawan, *Self-consistent cumulant expansion for the electron gas*, Physical Review B **56**, 12825 (1997).
- [34] B. Holm and U. von Barth, *Fully self-consistent GW self-energy of the electron gas*, Physical Review B **57**, 2108 (1998).
- [35] B. Holm and F. Aryasetiawan, *Total energy from the Galitskiĭ-Migdal formula using realistic spectral functions*, Physical Review B **62**, 4858 (2000).
- [36] G. F. Giuliani and G. Vignale, *Quantum theory of the electron liquid*, Cambridge Univ. Press, Cambridge, 2005.
- [37] B. I. Lundqvist, *Single-particle spectrum of the degenerate electron gas. I*, Physik der kondensierten Materie **6**, 193 (1967).
- [38] B. I. Lundqvist, *Single particle spectrum of the degenerate electron gas. II*, Physik der kondensierten Materie **6**, 206 (1967).
- [39] B. I. Lundqvist, *Single-particle spectrum of the degenerate electron gas*, Physik der kondensierten Materie **7**, 117 (1968).
- [40] M. Abramowitz and I. A. Stegun, editors, *Handbook of Mathematical Functions with Formulas, Graphs and Mathematical Tables*, Dover Publications, Inc., New York, 1965.
- [41] P. Virtanen, R. Gommers, T. E. Oliphant, M. Haberland, T. Reddy, D. Cournapeau, E. Burovski, P. Peterson, W. Weckesser, J. Bright, S. J. van der Walt, M. Brett, J. Wilson, K. J. Millman, N. Mayorov, A. R. J. Nelson, E. Jones, R. Kern, E. Larson, C. J. Carey, I. Polat, Y. Feng, E. W. Moore, J. VanderPlas, D. Laxalde, J. Perktold, R. Cimrman, I. Henriksen, E. A. Quintero, C. R. Harris, A. M. Archibald, A. H. Ribeiro, F. Pedregosa, and P. van Mulbregt, *SciPy 1.0: fundamental algorithms for scientific computing in Python*, Nature Methods **17**, 261 (2020).
- [42] C. L. Lawson and R. J. Hanson, *Solving Least Squares Problems*, Classics in Applied Mathematics, Society for Industrial and Applied Mathematics, 1995.
- [43] K.-H. Lee and K. J. Chang, *Analytic continuation of the dynamic response function using an N -point Padé approximant*, Phys. Rev. B **54**, R8285 (1996).
- [44] G. B. Thomas and M. D. Weir, *Calculus and Analytic Geometry*, Addison-Wesley, 1988.
- [45] F. Aryasetiawan and O. Gunnarsson, *The GW method*, Reports on Progress in Physics **61**, 237 (1998).
- [46] H. N. Rojas, R. W. Godby, and R. J. Needs, *Space-Time Method for Ab Initio Calculations of Self-Energies and Dielectric Response Functions of Solids*, Physical Review Letters **74**, 1827 (1995).

- [47] M. M. Rieger, L. Steinbeck, I. D. White, H. N. Rojas, and R. W. Godby, *The GW space-time method for the self-energy of large systems*, Computer Physics Communications **117**, 211 (1999).
- [48] A. L. Fetter and J. D. Walecka, *Quantum theory of many-particle systems*, McGraw-Hill, New York, 1971.
- [49] G. Giuliani and G. Vignale, *Quantum Theory of the Electron Liquid*, 2005.
- [50] L. N. Trefethen and J. a. C. Weideman, *The Exponentially Convergent Trapezoidal Rule*, SIAM Review **56**, 385 (2014).
- [51] T. Chiarotti and S. Vacondio and A. Ferretti, **AGWX** code suite.
- [52] A. L. Fetter and J. D. Walecka, *Quantum Theory of Many-particle Systems*, Courier Corporation, 2003.
- [53] F. Caruso and F. Giustino, *The GW plus cumulant method and plasmonic polarons: application to the homogeneous electron gas**, The European Physical Journal B **89**, 238 (2016).
- [54] C.-O. Almbladh, U. V. Barth, and R. V. Leeuwen, *Variational total energies from phi- and psi- derivable theories*, International Journal of Modern Physics B **13**, 535 (1999).
- [55] J. P. Perdew and A. Zunger, *Self-interaction correction to density-functional approximations for many-electron systems*, Physical Review B **23**, 5048 (1981).
- [56] D. M. Ceperley and B. J. Alder, *Ground State of the Electron Gas by a Stochastic Method*, Physical Review Letters **45**, 566 (1980).
- [57] See Supplemental Material for a detailed description of the convergence studies and the numerical parameters adopted to perform the HEG calculations.

Supplemental Material

A unified Green's function approach for spectral and thermodynamic properties from algorithmic inversion of dynamical potentials

Tommaso Chiarotti,^{1,*} Nicola Marzari,¹ and Andrea Ferretti²¹*Theory and Simulations of Materials (THEOS) and National Centre for Computational Design and Discovery of Novel Materials (MARVEL), École Polytechnique Fédérale de Lausanne, 1015 Lausanne, Switzerland*²*Centro S3, CNR-Istituto Nanoscienze, 41125 Modena, Italy*

(Dated: September 17, 2021)

This manuscript contains the supplemental material for the paper: “A unified Green's function approach for spectral and thermodynamic properties from algorithmic inversion of dynamical potentials”.

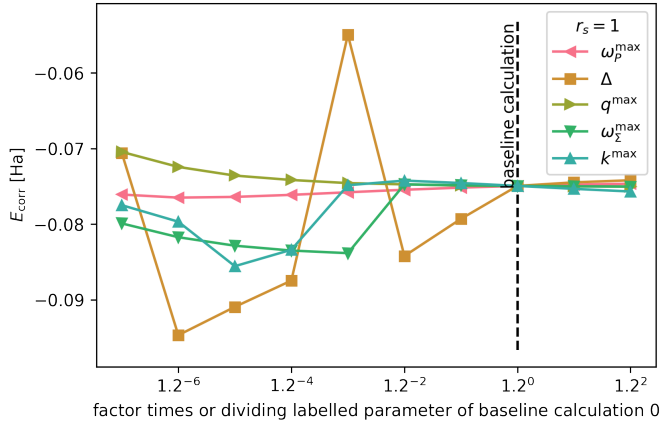


FIG. 1. Correlation energy E_{corr} convergence study obtained with the Galitzki-Migdal formula using a Green function from a G_0W_0 calculation for the HEG at $r_s = 1$. See Fig. 5 of [1] for further reference.

I. CONVERGENCE STUDIES AT SEVERAL DENSITIES OF THE HEG

In this section we show the convergence studies at all densities of [1]. Following the method presented in Secs. III, and particularly III C, of [1] at $r_s = 4$, we study stability and convergence of the correlation (total minus Fock) energy per particle at r_s from 1 to 10. In Figs. 1, 2, 3, 4, 5, 6, 7, 8, 9, 10 we plot the convergence study at the different densities.

- [1] T. Chiarotti, N. Marzari, and A. Ferretti, *A unified Green's function approach for spectral and thermodynamic properties: Application to the electron gas*, XXX (XXX).

* corresponding author: tommaso.chiarotti@epfl.ch

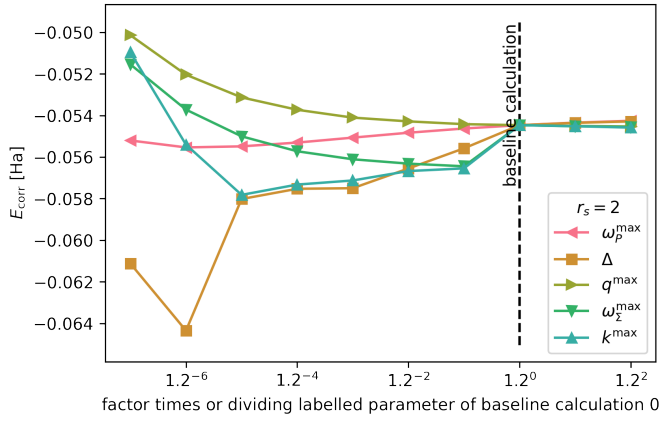


FIG. 2. Correlation energy E_{corr} convergence study obtained with the Galitzki-Migdal formula using a Green function from a G_0W_0 calculation for the HEG at $r_s = 2$. See Fig. 4 of [1] for further reference.

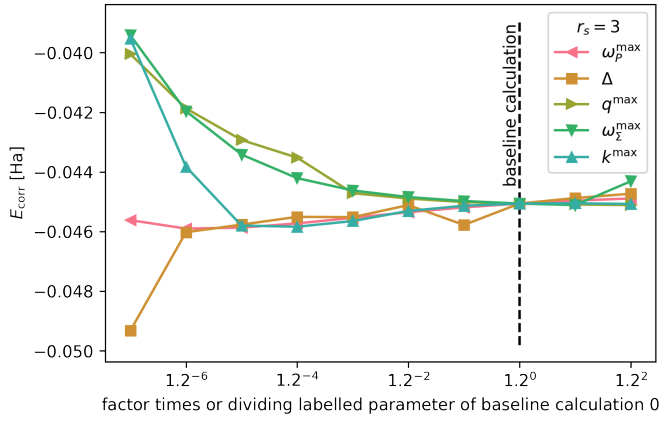


FIG. 3. Correlation energy E_{corr} convergence study obtained with the Galitzki-Migdal formula using a Green function from a G_0W_0 calculation for the HEG at $r_s = 3$. See Fig. 5 of [1] for further reference.

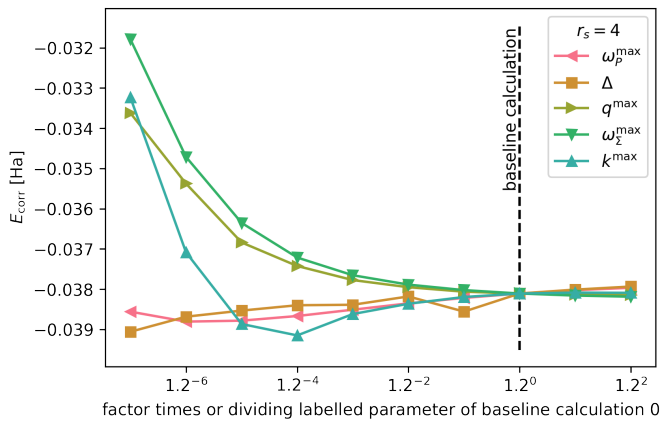


FIG. 4. Correlation energy E_{corr} convergence study obtained with the Galitzki-Migdal formula using a Green function from a G_0W_0 calculation for the HEG at $r_s = 4$. See Fig. 5 of [1] for further reference.

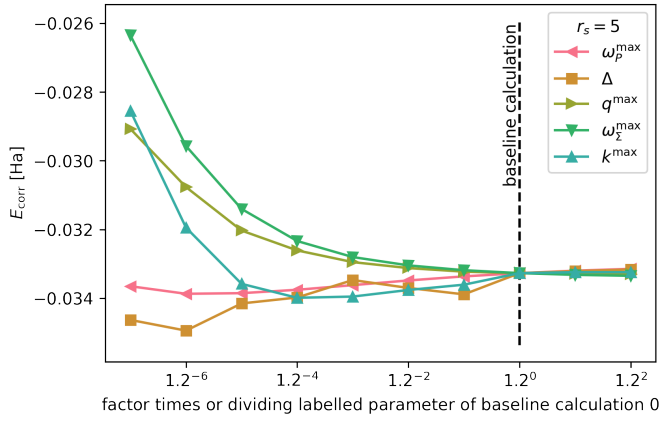


FIG. 5. Correlation energy E_{corr} convergence study obtained with the Galitzki-Migdal formula using a Green function from a G_0W_0 calculation for the HEG at $r_s = 5$. See Fig. 5 of [1] for further reference.

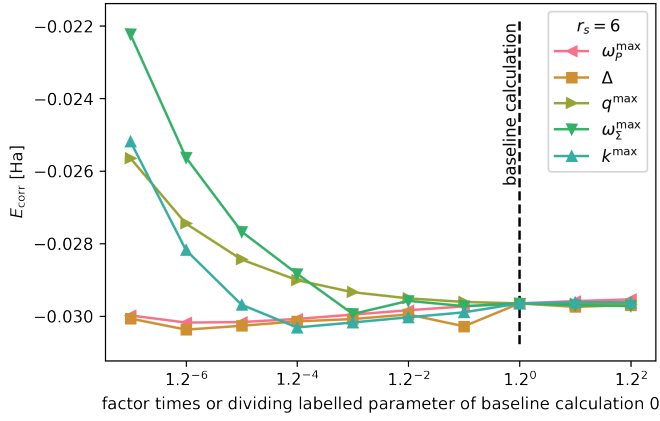


FIG. 6. Correlation energy E_{corr} convergence study obtained with the Galitzki-Migdal formula using a Green function from a G_0W_0 calculation for the HEG at $r_s = 6$. See Fig. 5 of [1] for further reference.

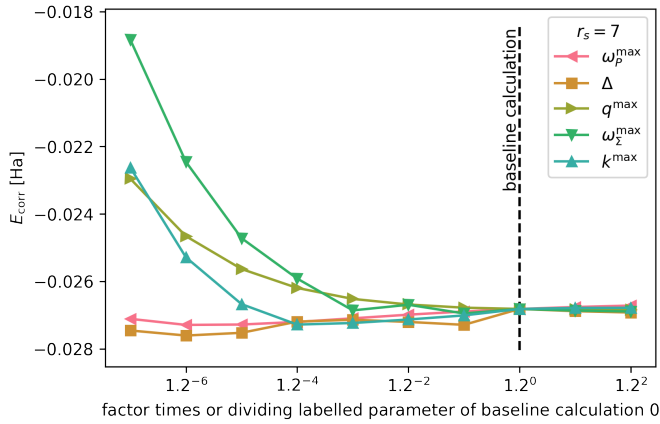


FIG. 7. Correlation energy E_{corr} convergence study obtained with the Galitzki-Migdal formula using a Green function from a G_0W_0 calculation for the HEG at $r_s = 7$. See Fig. 5 of [1] for further reference.

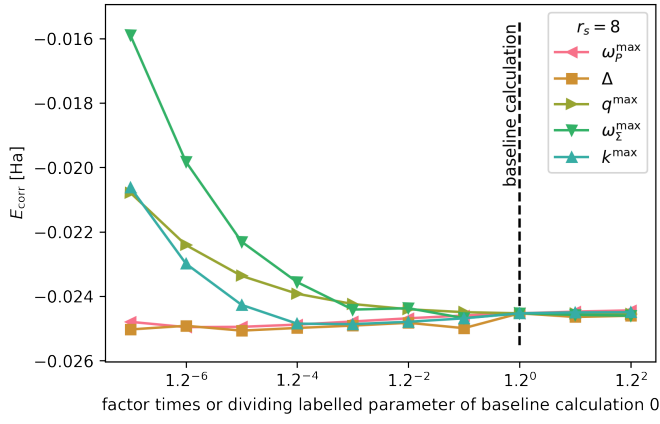


FIG. 8. Correlation energy E_{corr} convergence study obtained with the Galitzki-Migdal formula using a Green function from a G_0W_0 calculation for the HEG at $r_s = 8$. See Fig. 5 of [1] for further reference.

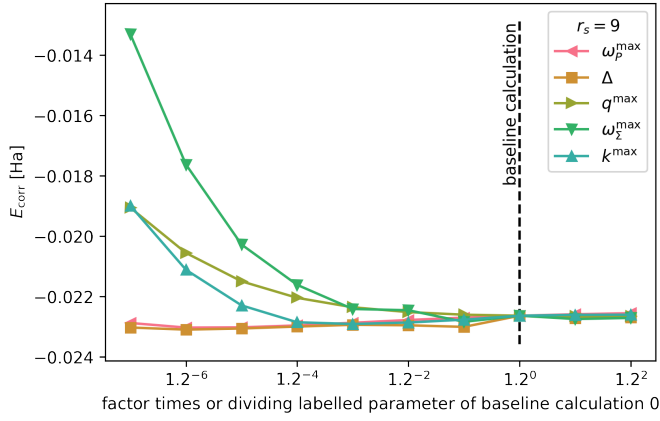


FIG. 9. Correlation energy E_{corr} convergence study obtained with the Galitzki-Migdal formula using a Green function from a G_0W_0 calculation for the HEG at $r_s = 9$. See Fig. 5 of [1] for further reference.

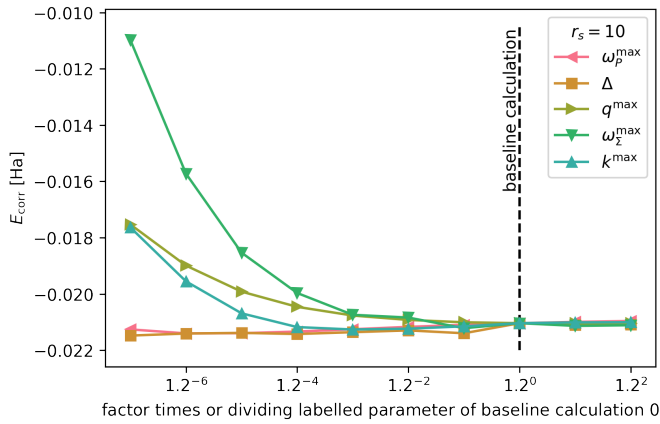


FIG. 10. Correlation energy E_{corr} convergence study obtained with the Galitzki-Migdal formula using a Green function from a G_0W_0 calculation for the HEG at $r_s = 10$. See Fig. 5 of [1] for further reference.